# Guiding bone cell network formation in 3D via photosensitized two-photon ablation

**Author(s):**
Gehre, Christian; Qiu, Wanwan; Jäger, Patrick Klaus; Wang, Xiaopu; Correira Marques, Francisco; Nelson, Bradley (iD); Müller, Ralph (iD); Qin, Xiao-Hua (iD)
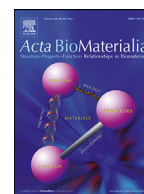
Full length article

# Guiding bone cell network formation in 3D via photosensitized two-photon ablation

Christian Gehre[a], Wanwan Qiu[a], Patrick Klaus Jäger[a], Xiaopu Wang[b], Francisco Correia Marques[a], Bradley J. Nelson[b], Ralph Müller[a], Xiao-Hua Qin[a,*]

[a] *Institute for Biomechanics, ETH Zurich, Zürich, Switzerland*
[b] *Institute of Robotics and Intelligent Systems, Zürich, Switzerland*

### ARTICLE INFO

### ABSTRACT

A long-standing challenge in skeletal tissue engineering is to reconstruct a three-dimensionally (3D) interconnected bone cell network *in vitro* that mimics the native bone microarchitecture. While conventional hydrogels are extensively used in studying bone cell behavior *in vitro*, current techniques lack the precision to manipulate the complex pericellular environment found in bone. The goal of this study is to guide single bone cells to form a 3D network *in vitro* via photosensitized two-photon ablation of microchannels in gelatin methacryloyl (GelMA) hydrogels. A water-soluble two-photon photosensitizer (P2CK) was added to soft GelMA hydrogels to enhance the ablation efficiency. Remarkably, adding 0.5 mM P2CK reduced the energy dosage threshold five-fold compared to untreated controls, enabling more cell-compatible ablation. By employing low-energy ablation ($100\ J/cm^2$) with a grid pattern of 1 μm wide and 30 μm deep microchannels, we induced dendritic outgrowth in human mesenchymal stem cells (hMSC). After 7 days, the cells successfully utilized the microchannels and formed a 3D network. Our findings reveal that cellular viability after low-energy ablation was comparable to unablated controls, whereas high-energy ablation ($500\ J/cm^2$) resulted in 42 % cell death. Low-energy grid ablation significantly promoted network formation and $>40$ μm long protrusion outgrowth. While the broad-spectrum matrix metalloproteinase inhibitor (GM6001) reduced cell spreading by inhibiting matrix degradation, cells invaded the microchannel grid with long protrusions. Collectively, these results emphasize the potential of photosensitized two-photon hydrogel ablation as a high-precision tool for laser-guided biofabrication of 3D cellular networks *in vitro*.

**Statement of Significance**

The inaccessible nature of osteocyte networks in bones renders fundamental research on skeletal biology a major challenge. This limit is partly due to the lack of high-resolution tools that can manipulate the pericellular environment in 3D cultures *in vitro*. To create bone-like cellular networks, we employ a two-photon laser in combination with a two-photon sensitizer to erode microchannels with low laser dosages into GelMA hydrogels. By providing a grid of microchannels, the cells self-organized into a 3D interconnected network within days. Laser-guided formation of 3D networks from single cells at micronscale resolution is demonstrated for the first time. In future, we envisage *in vitro* generation of bone cell networks with user-dictated morphologies for both fundamental and translational bone research.

## 1. Introduction

*In vitro* generation of functional human tissues with native-like microarchitectures has become the focus in regenerative medicine [1]. Such *in vitro* models provide the means to investigate fundamental questions in tissue formation and accelerate drug screenings of patient-specific therapies with minimal reliance on animal models. Existing 3D *in vitro* models rely on the embedding of cells, such as stem cells, in extracellular matrix (ECM)-resembling hydrogels [2]. In bone, the soft osteoid matrix encases osteoblasts during early osteogenesis, where they differentiate into an osteo-

---

* Corresponding author at: Gloriastrasse 39, 8092 Zürich, Switzerland.
*E-mail address:* qinx@ethz.ch (X.-H. Qin).

cyte network that is enclosed within the lacunar-canalicular network (LCN). By permeating this sophisticated network of cavities and microscopic channels with a multitude of dendrites, osteocytes function as mechanosensory cells that orchestrate the bone remodeling process in response to mechanical load [3,4]. Therefore, a functional LCN is crucial to maintain bone's structural integrity. However, as individuals age, deterioration of the osteocyte network impacts bone adaptation to mechanical forces [5,6]. Key characteristics of an aged LCN include a reduced number of osteocytes and progressed dendrite deterioration, leading to decreased cellular connectivity and weakened structural strength of bone. Thus, developing techniques to mimic the LCN *in vitro* may enrich our fundamental understanding of how these microstructures play a role in bone diseases such as age-related bone loss [7]. Whilst previous work has explored 3D osteogenic culture [8] of immortalized murine bone cells in low stiffness (0.58 kPa) gelatin-based hydrogels [9], between glass microbeads [10], and in bioprinted constructs [11], the presented dendritic phenotype does not resemble the cellular network *in vivo*. This is partly due to the usage of genetically modified cell lines and, most importantly, due to the lack of canalicular structures that enhance cell spreading.

Recent progress in microfabrication has enabled exquisite control over a biomaterial's microarchitecture in 3D [12–14]. Two-photon micropatterning has proven to be an effective tool for high-resolution structuring of hydrogels through additive (two-photon-induced polymerization [15–17]) or subtractive processes (two-photon-induced ablation or degradation [12,18]). In materials with a high content of natural fibers, such as gelatin, controlled photoablation is based on the laser-directed deposition of energy within the focal spot. Short laser pulses in the range of femtoseconds create confined heat and cause plasma generation, leading to the breakdown of hydrogen and protein bonds [19]. For instance, Sarig-Nadir et al. utilized a custom two-photon laser setup to ablate a path for embedded neuronal cells to migrate into their confined surrounding [18]. Subsequent work focused on light-induced degradation in synthetic photosensitive materials [12,20] or photografting. For instance, Sayer et al. demonstrated the use of 4,4′-diazido-2,2′-stilbenedisulfonic acid (DSSA) as a photografting agent in gelatin methacryloyl (GelMA) hydrogels in the presence of cell clusters to direct cell growth *in vitro* [21]. Given that collagen accounts for 80 % of bone's protein content [22], we selected photocrosslinkable collagen-derived GelMA because of its tuneability, biodegradability and ease-of-use for bone *in vitro* models. Surprisingly, Xiong et al. observed a laser dosage dependent shift from densification to ablation upon two-photon micropatterning in partially crosslinked GelMA matrices, where embedded cells showed basic alignment with the densified patterns [23]. Although previous studies predominantly focused on providing physical cues to clustered cells, two-photon micropatterning of single bone cells remains largely unexplored. Individual cells, opposed to clustered cells, resemble the *in vivo* environment of osteocytes more faithfully, where the mean nearest neighbor distance was reported to be around 23 μm (femoral cortical bone) [24].

For the ambition of two-photon biofabrication in the presence of cells, strategies to reduce the applied laser dosage are extensively sought after. Recently, Li et al. introduced a set of highly efficient water-soluble two-photon photoinitiators, among them P2CK (sodium 3,3′-((((1E,1′E)-(2-oxocyclopentane-1,3-diylidene)-bis(methaneylylidene))-bis(4,1-phenylene))-bis(methylazanediyl))-dipropionate) with a large two-photon absorption cross-section (176 GM in water at 800 nm) for 3D microfabrication of PEG diacrylate hydrogels [25]. Ovsianikov et al. reported the first attempt of P2CK-initiated two-photon polymerization in the presence of cells in GelMA, where cytotoxicity remained an issue [15,26]. Contrarily, Lunzer et al. successfully exploited P2CK as a photosensitizer to decrease the laser power for two-photon

photodegradation in *o*-nitrobenzyl ester-containing polyethylene glycol (PEG)-hyaluronan (HA) hydrogels in the presence of immortalized adipose-derived mesenchymal stem cell clusters [12]. The photosensitizing effect of P2CK allows to use a higher scanning speed at a lower laser power, thus reducing the laser dosage and enhancing the cell-compatibility during two-photon degradation.

Here, we employ laser-guided and P2CK-sensitized two-photon ablation in soft GelMA hydrogels to create microchannels that facilitate the formation of bone cell networks in 3D *in vitro* culture. To reach this goal, we use soft GelMA hydrogels to provide a permissive osteoid-resembling matrix for embedded single hMSC. The efficiency of photosensitized ablation was confirmed by perfusing ablated microchannels with a fluorescent tracer, identifying the minimum laser dosage for successful ablation. After microchannel ablation in the presence of single cells, cell compatibility and cellular network formation were determined by fluorescent staining and image analysis following osteogenic culture for 14 days. For a mechanistic understanding of cellular network formation, we assessed the effects of inhibiting proteolytic matrix degradation on guided cell spreading. Using photosensitized two-photon ablation of microchannels, we aim to guide cellular outgrowth towards an interconnected 3D bone cell network for future applications in fundamental and translational research in bone biology.

## 2. Materials and methods

### 2.1. Materials development

The synthesis and characterization of GelMA precursor and two-photon sensitizer (P2CK) are provided in the Supporting Information.

### 2.2. Photorheology

To characterize the mechanical properties of GelMA, stock solutions of 10 or 20 % (w/v) GelMA in 0.1 % Lithium phenyl-2,4,6-trimethylbenzoylphosphinate (LAP) were prepared and prior to measurement diluted with PBS to final concentrations of 5 and 10 % GelMA in 0.05 % LAP. For *in-situ* photo-rheology, the solution was pipetted on the bottom glass plate on a rheometer (MCR 302, Anton Paar, Graz, Austria), equipped with a 20 mm measuring plate and pre-installed UV-lamp for sample irradiation at 10 mW/cm$^2$ and 365 nm. With the working distance set to 0.1 mm, ambient temperature of 25 °C, and measurements set to 1 Hz under 0.5 % strain, time-lapsed evolution of storage (G′) and loss modulus (G″) of the GelMA solutions were determined during crosslinking (Fig. 1b). The UV-light was turned on after 60 s followed by *in situ* photocrosslinking for 5 min.

### 2.3. Mass swelling ratio

To test the mass swelling ratio (SR) of GelMA, the wet weight ($M_w$) of hydrogels swollen in PBS for 14 days to simulate culture conditions was determined and divided by dry weight ($M_d$), which was obtained by lyophilizing the same gels and weighing the remains.

$$SR = \frac{M_w}{M_d} \times 100\%$$

### 2.4. Cell culture

Human mesenchymal stem cells (PT-2501, Lonza, Walkersville, MD, USA) isolated from donated human tissue, were grown in expansion medium, consisting of DMEM, 10 % FBS, 1 % Antibiotic-Antimycotic, 1 % non-essential amino acids, and 0.001 % basic fibroblast growth factor. The osteogenic potential of the obtained
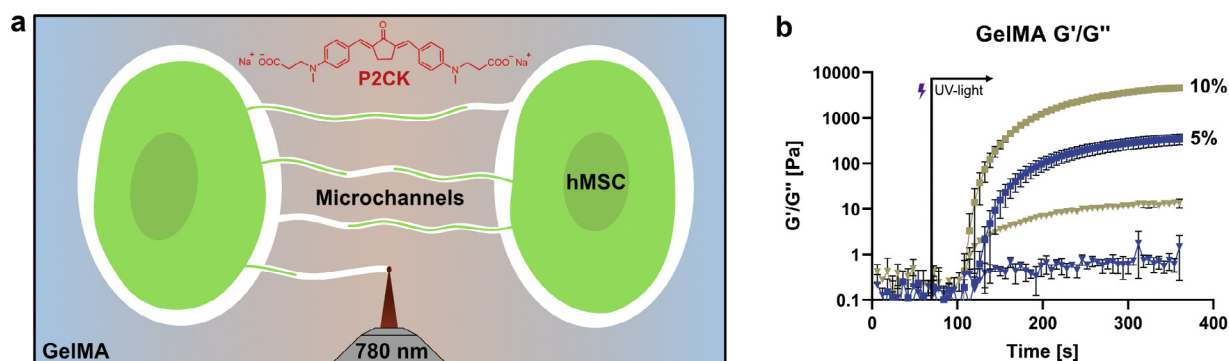
**Fig. 1.** Schematic of laser-guided cellular network formation by photosensitized two-photon ablation. (a) Bone cells embedded in photocrosslinked GelMA hydrogels are submerged in a solution containing the two-photon sensitizer P2CK for ablation. The high-precision setup of a two-photon laser mounted to a confocal microscope is utilized to carve hollow microchannels between the embedded hMSC. The otherwise constrained cells spread into the microchannels and form a cellular network. (b) To determine the mechanical properties of 5 % and 10 % GelMA (w/v), the storage (G', squares) and loss (G'', triangles) modulus during photocrosslinking ($n = 3$) were measured via *in situ* photo-rheology (365 nm, 10 mW/cm²) with a strain of 0.5 % and frequency at 1 Hz. Light was turned on at 60 s.

hMSC was certified prior to the purchase. Briefly, cells were expanded until they reached confluence with media change every 2 days, detached with Trypsin-EDTA, and used for further cultivation or experiments directly. Experiments were conducted with a cell passage number between 4 and 8. After ablation, cells were cultivated in osteogenic conditions for up to 14 days using a differentiation medium consisting of DMEM, 10 % FBS, 1 % Antibiotic-Antimycotic, 50 µg/ml ascorbic acid, 100 nM Dexamethasone, 10 mM beta-glycerophosphate was used. Osteogenic medium was changed every two days.

### 2.5. Gel casting

For gel casting (Fig. S1), the GelMA precursor solution (10 % or 20 % GelMA in 0.1 % LAP) was prepared and warmed to 37 °C. Prior to each experiment, 13 mm glass cover slips were hydrophobized with Sigmacote (Sigma Aldrich, SL2) and sterilized by irradiation with 265 nm UV-light. Molds were prepared by cutting 4 mm diameter wells with a biopsy punch in 0.5 mm thick silicone mats (McMaster-Carr, Elmhurst, IL, USA) and subsequent sterilization in 70 % ethanol for at least 10 min. For mold assembly, the silicone molds were placed on 30 mm glass coverslips (#1.5) or confocal dishes (VWR, Radnor, PA, USA). In the meantime, the precursor solution was diluted with PBS to the final concentration (5 % or 10 % GelMA in 0.05 % LAP) and transferred into the wells of the mold. After covering the top of the wells with the coated coverslips, the molds were irradiated with 365 nm UV-light for 5 min. With a power meter (Thorlabs, Dachau, Germany), the UV-light intensity was adjusted before each experiment to 10 mW/cm². The molds were then soaked in PBS and disassembled so that the gels stay attached to the bottom cover glass. For cellular samples, the precursor GelMA solution was thoroughly mixed with the desired number of cells in PBS. For this study, the final cell concentration was adjusted to 2.5 million cells/ml. For acellular experiments, the sterilization steps were skipped.

### 2.6. Two-photon ablation

Two-Photon ablation was conducted on a Leica SP8-MP confocal microscope (Leica, Wetzlar, Germany). Specifically, a Mai Tai XF two-photon laser (Spectra-Physics, Milpitas, CA, USA) with tuneable wavelength and a pulse width of < 80 fs was used. Preformed gels were washed once with PBS and then submerged in a solution of 0.5 mM P2CK (Fig. S2) in PBS for 15–30 min (control: PBS) before two-photon ablation. Prior to ablation, the laser power at the objective was measured using a power meter and adjusted to a fixed value of 100 mW. When cellular samples were patterned, the

climate chamber was kept at 37 °C to provide cell friendly conditions. As described elsewhere [23], the laser energy dosage was defined as:

$$E = \frac{P}{\pi \left( \frac{0.61\lambda}{NA} \right)^2} \times \frac{\frac{1.22\lambda}{NA}}{V}$$

where $P$ is the laser power measured directly at the objective, $\lambda$ the wavelength of the two-photon laser (780 nm), *NA* the numerical aperture of the objective (40x, Leica HC PL IRAPO, NA 1.1), and $V$ the scanning speed of the laser.

Different laser dosages were achieved by varying the scanning speed. Using the region-of-interest function of the LASX software, custom shapes such as singular channels or a grid of microchannels with defined dimensions (1 µm in diameter, 40 µm distance between horizontal and vertical channels within the grid) were fabricated. Patterns were ablated at a depth of approximately 70 µm into the sample. To extrude the planar shapes into 3D, the z-stack function of the microscope was used to continuously ablate through the z-axis (channel dimension: 1 µm wide, 30 µm in depth). Cellular samples were processed within 1 hour after incubation with P2CK solution to prevent possible cytotoxicity of prolonged exposure. After ablation, all samples were thoroughly washed three times in PBS and either cultivated in osteogenic conditions or stored at 4 °C for acellular samples until further processing.

### 2.7. Visualization of ablated microchannels

#### 2.7.1. Fluorescence-intensity-based measurement of ablation efficiency

To compare the efficiency of two-photon ablation, microchannels with dimensions of 5 × 5 × 200 µm were ablated in 5 % GelMA gels, either treated or untreated with P2CK. For ablation, energy dosages of 50, 100, 200, 300, 400, and 500 J/cm² were used to pattern 10 channels per dosage for each sample (3 replicates). After repeated washing and overnight incubation in PBS, the gels were submerged in a 1 % (w/v) solution of 2000 kDa FITC-dextran (Merck, Darmstadt, Germany) and incubated overnight. Z-stack images of the dye-perfused channels were acquired on a Leica SP8-AOBS confocal microscope with a 25x objective. To measure the degree of ablation, the fluorescence intensity of FITC-dextran tracer molecules within each channel was measured in FIJI by transforming the acquired z-stacks into maximum intensity projections and drawing a region of interest that covers the entire channel. Intensity values of 10 channels per dosage per sample ($n = 3$) were averaged and displayed as means ± standard deviation. The results were analyzed with GraphPad Prism (GraphPad Software, USA) us-

ing unpaired *t*-tests to compare P2CK-treated and untreated samples for each dosage. To label the bulk matrix instead of the ablated channel lumen, samples were stained with 0.1 % (w/v) thiolated FITC that binds to the residual methacrylate groups in preformed GelMA matrix by thiol-Michael addition. After 1 hour incubation in the dark, samples were washed three times for 5 min in PBS and stored at 4 °C until imaging.

### 2.7.2. Fluorescence recovery after photobleaching (FRAP)

FRAP was conducted in a 5 % GelMA gel that was ablated with a microchannel grid (1 µm wide, 30 µm deep) using 0.5 mM P2CK at a depth of 50 µm into the gel. After subsequent washing in PBS (48 h) to remove remaining P2CK, the constructs were submerged in a 1 % (w/v) solution of FITC-dextran ($M_w$, 2000 kDa) and incubated overnight. FRAP was executed on a Zeiss LSM 780 confocal microscope (Carl Zeiss AG, Oberkochen, Germany) by utilizing a 488 nm laser for imaging and bleaching. While maintaining acquisition, a region of interest within the grid (node or channel) was bleached for 5–10 s after an initial waiting period of 15 s and imaged until a steady fluorescence signal was reached. The controls were chosen to be near the bleaching site. The positive control was located within the grid whereas the background control was in the non-ablated region between channels.

### 2.8. Immunofluorescence

### 2.8.1. Cell viability

Cell viability, cell morphology, and biomarker expression were observed with different fluorescent stains. To assess cell viability after patterning, a cell viability kit (ab176749, Abcam, Cambridge, UK) outside the fluorescent emission range of P2CK was used, due to the non-specific binding of P2CK to the matrix at the laser ablated sites. After ablating 3D microchannel grids with 100, 300, and 500 J/cm$^2$ in 0.5 mM P2CK ($n = 3$), cells were kept in control medium (DMEM supplemented with 10 % FBS, 1 % Antibiotic-Antimycotic) for 24 h before viability assessment. Viable, apoptotic, and necrotic cells were stained in PBS for 40 min at room temperature in the dark. After 3x washing in PBS, the cells were imaged on a Leica SP8-MP confocal microscope. Due to the remaining background signal from autofluorescent photoactive materials (LAP and P2CK) and early cell spreading into the channels, the number of cells had to be counted manually using the FIJI cell counter plugin. The apoptotic and necrotic cells were summarized as dead cells and transformed into live-dead ratio per grid. In addition to staining the cytoplasm of viable cells with CytoCalcein violet 450, apoptotic cells are labelled via Apopxin Green that binds the membrane-bound apoptotic marker phosphatidylserine. To differentiate apoptotic from necrotic cells, the kit includes the membrane-impermeable nucleus labelling dye 7-AAD, which can only penetrate the cell membrane of necrotic cells. Ratios were averaged per condition and displayed as means ± standard deviation. The results were analyzed with GraphPad Prism using one-way Anova.

### 2.8.2. Cell morphology and biomarkers

To visualize the cell morphology, samples were fixed and stained for f-actin and nuclei. For fixation, samples were incubated in 4 % paraformaldehyde for 20 min at room temperature and subsequently washed 4x with PBS. Until further processing, the samples were sealed with parafilm and stored at 4 °C. For immunocytochemistry stains the samples were first permeabilized using 0.2 % triton X-100 in PBS for 20 min at RT and washed twice for 2 min in PBS. Afterwards, samples were blocked in 1 % BSA for 1 h at RT. If alkaline phosphatase (MAB1448, R&D Systems, Minneapolis, MN, USA) or connexin-43 (sc-271837, Santa Cruz Biotechnologies, Dallas, TX, USA) antibodies were used, the primary antibodies were incubated overnight at 4 °C in 0.1 % BSA in PBS in a 1:200 dilution. After three times washing in PBS for 2 min, either an Alexa Fluor 488 (A21202, Thermo Fisher Scientific, Waltham, MA, USA) or Alexa Fluor 647 (ab150075, Abcam, Cambridge, UK) coupled secondary antibody was incubated 1:200 in 0.1 % BSA in PBS for 1 h at RT. Following three PBS washing steps for 2 min, either TRITC-(P1951, Merck, Darmstadt, Germany) or Alexa Fluor 647 (ab176759, Abcam, Cambridge, UK) coupled Phalloidin was used in combination with Hoechst in a 1:500 dilution to stain f-actin and nuclei. Samples were imaged directly after staining or stored at 4 °C until further use. Mineral was stained using an OsteoImage staining kit (PA-1503, Lonza, Basel, CH).

### 2.9. Network analysis

### 2.9.1. 3D network length quantification

Z-Stacks of actin-nuclei stained samples were processed and analysed with a custom-made script [27]. In short, the length of cellular networks was measured by skeletonizing the actin signal from maximum intensity projections and normalized to the cell count of each sample ($n = 2$–3). Due to natural spreading of the embedded cells in the surrounding bulk matrix after embedding, measured branch length of below 20 µm were excluded from the analysis. The resulting network length per cell was used as an indicator for cell spreading behaviour. Histograms of the branch length and count were plotted by applying a bin size of 8 to observe the effect of sensitization (Fig. 5) and 12 for the GM6001 perturbation study (Fig. 6).

### 2.9.2. Manual counting of guided cell outgrowth

To determine the degree of occupation of the patterned microchannel grid, the number of cellular protrusions that grew into the microchannels were counted and divided by the number of channels. To count the number of channels, each channel-segment between two intersecting points was counted as a singular channel and assigned to one of the following orientations: horizontal, vertical, diagonal 1 (bottom-left to top-right), diagonal 2 (top-left to bottom-right) (Fig. 4b). Using maximum intensity projections of actin-stained samples, every channel occupied by a cell protrusion was counted using FIJI. Intensity thresholds were kept the same for all samples.

### 2.10. Statistical analysis

GraphPad Prism 10 was used to perform the statistical analysis for the obtained data. Cell viability was analyzed using a one-way ANOVA test together with multiple comparisons. The network length per cell, fluorescence intensity after ablation, and ALP expression were compared between groups at different timepoints using a two-way ANOVA with multiple comparisons. *p < 0.05 were considered statistically significant.

## 3. Results

### 3.1. Photosensitized two-photon ablation in GelMA hydrogels

Laser ablation occurs due to the high energy delivered in short pulses, leading to electron excitation and thus the localized dispersion of disruptive energy [28]. An efficient two-photon photosensitizer (P2CK [25]), has been employed to significantly reduce the amount of laser dosage necessary to achieve two-photon photodegradation and polymerization of photosensitive materials [12,15,29]. In this study, we hypothesized that P2CK can significantly reduce the laser dosage for two-photon ablation and enhance its cell-compatibility, thereby enabling microchannel fabrication during 3D cell culture. To establish a protocol for photo-

**Table 1**
Physical properties of GelMA hydrogels. The gel moduli and mass swelling ratio of 5 % and 10 % GelMA hydrogels; mean values ± standard deviation.

| GelMA [%] | G' [Pa] | G" [Pa] | Swelling Ratio |
|---|---|---|---|
| 5 % | 350.9 ± 93.2 | 1.5 ± 1.2 | 20.2 ± 4.8 |
| 10 % | 4662.0 ± 515.8 | 13.7 ± 3.1 | 13.0 ± 1.0 |

sensitized two-photon ablation, the physical properties of hydrogels as well as the experimental setup during laser ablation need to be defined. In our study design (Fig. 1a), we firstly use *in situ* UV photocrosslinking to embed single hMSC cells in a mm-scale GelMA hydrogel in 3D. The samples were then soaked in a solution of photosensitizer P2CK (0.5 mM) and mounted on a commercial two-photon confocal microscope equipped with a femtosecond pulsed two-photon laser. This setup allows localized two-photon excitation at 780 nm to ablate the hydrogel matrix and carve micrometer-scale channels *in situ*. The channels provide an opening to the cells within the otherwise confining matrix, leading to the growth of cell protrusions and eventually a 3D cellular network. To investigate the mechanical properties of the hydrogels, photo-rheology was conducted to determine the storage and loss moduli during *in situ* photocrosslinking. The hydrogels exhibit a storage modulus (G') of *ca.* 4662 Pa and 350 Pa upon crosslinking at 10 % and 5 %, respectively (Fig. 1b, Table 1).

The gel dimensions are approximately 3 mm in diameter and 1 mm thick. Literature shows that 5 % GelMA is permeable for cell culture medium to maintain viable cells in up to 3 mm depth [30]. Since soft hydrogel matrices have been shown to enhance osteogenic differentiation in 3D cultures [9,31], 5 % (w/v) GelMA was from here on used as a platform for sensitized ablation in the presence of cells. It was hypothesized that a softer matrix with less dense networks offers higher efficiency for laser ablation.

Here, we use the energy dosage "*E*" to describe the laser output into the material [23,28]. The calculated dosage considers the initial laser power measured at the sample position, as well as the exposure time within the focal spot, and thus describes the energy that is applied during patterning. To show the effect of P2CK mediated two-photon ablation in GelMA, ablated microchannels were perfused with a fluorescent tracer (FITC-dextran, 2 MDa).

The microchannels were ablated with increasing laser dosage, while being submerged in 0–1 mM P2CK solutions. Subsequent immersion with a fluorescent dye (FITC-dextran) allows to visualize the channel fidelity and to utilize the fluorescence intensity as a readout for ablation efficiency (Fig. 2a). The diffusion of FITC-dextran depends on the degree of ablation and thus permeability within the ablated channels. The hydrodynamic size of the tracer molecules leads to diffusion into the hollow channels instead of the unablated hydrogel matrix. The perfused microchannels displayed a sharp channel outline with a strong fluorescent signal when 0.5 mM or 1 mM P2CK was used during ablation down to 100 J/cm² (Fig. 2b) Conversely, 0.1 mM P2CK and negative control (0 mM P2CK) resulted in a significantly decreased intensity. Measuring the fluorescence intensity to quantify the ablation efficiency, higher P2CK concentrations showed an overall significantly improved ablation, compared to low concentrations (Fig. 2c). As for ablation in the presence of 0.5 mM, a significant drop in fluorescence intensity was only measured below 100 J/cm², indicating the feasibility of low-dosage ablation. Therefore, 100 J/cm² was determined as the optimal laser dosage in combination with 0.5 mM P2CK for further cellular experiments. Furthermore, higher P2CK concentrations (1 – 4 mM) have been shown to negatively affect cell viability for prolonged exposure (24 h) without laser irradiation [26]. Permeability of the microchannels after ablation with 100 J/cm² was demonstrated using FRAP on a FITC-dextran

perfused microchannel grid (Fig. 2d,e). Fluorescence recovery was achieved within 2 min after bleaching, both in a grid node as well as in a channel.

Further examination of ablating smaller channels confirmed that 1 µm in diameter channels can be printed with similar fidelity (Fig. S5). In contrast to the previous experiment, the sample was not perfused with FITC-dextran after ablation but instead covalently labelled with a thiolated FITC dye to stain the solid bulk matrix. The ablated channel lumen therefore appears as black line within the otherwise intact soft GelMA matrix, as it is visible in all dosages from 100 – 550 J/cm². The stiffer 10 % GelMA sample instead appears brighter around the channel circumference, indicating a local densification of the hydrogel matrix in the presence of residual photocrosslinkable groups. Notably, laser-induced densification has been reported previously in partially crosslinked 7–10 % GelMA matrices [23]. Taken together, these results indicate the feasibility of P2CK for low-energy ablation, which is desirable for two-photon micropatterning in the presence of cells.

### 3.2. Patterning in the presence of cells

#### 3.2.1. Guided cell outgrowth from a single plane

For proof-of-concept laser-guided cell outgrowth, we utilized the region-of-interest function of a multiphoton microscope to introduce planar 1 µm microchannels between hMSC clusters inside a GelMA hydrogel. As shown in Fig. S6a, the relatively high laser dosage (550 J/cm²) did not deter cellular outgrowth and migration into the microchannels. Although the cells can actively degrade the matrix and pursue undirected spreading and migration, the ablated microchannels induced the formation of over 100 µm long cell protrusions. Remarkably, the cells reshaped the microchannels to fit the entire cell body. The scale of cell-matrix interactions becomes apparent when observing cell spreading via holotomography (Fig. S6b). Due to its refractive index-based imaging, holotomography revealed small features with otherwise low contrast [32]. Thus, the bent and elongated cells appear bright and detailed within the microchannels.

In native bone tissue, individual osteocytes are interconnected in 3D within the bone matrix rather than clusters. Therefore, a grid of microchannels was ablated in the presence of embedded hMSC with a slightly lower dosage of 400 J/cm² (Fig. 3a). Already within 24 h after patterning, the cells started to spread into the microchannels to form cell-cell connections, as visualized by actin-nuclei staining. After 7 days, cell protrusions stretched over several hundred micrometers into the microchannels, precisely resembling the grid morphology. Cell bodies were fully integrated into the channels, alongside bent nuclei and cell organelles. The gap junction marker Connexin 43 was expressed on the cell bodies, as well as the protrusions within the channels (Fig. 3b), demonstrating the formation of functional intercellular connections within the grid. Altogether, these results highlight how sensitized two-photon ablation can guide embedded hMSC to form arbitrarily shaped, interconnected cellular networks within a prescribed single plane of microchannels.

#### 3.2.2. Guided cell outgrowth using a 3D grid

To guide cell outgrowth in 3D, the previously designed grid was extruded to have a depth of 30 µm and include additional diagonal microchannels (Fig. 4a, i-ii). During osteogenic cultivation, the cells extended into the 3D grid and formed a cellular network that eventually closely resembles the grid morphology (Fig. 4a, iii). When quantifying cellular outgrowth in relation to the channel orientation, no significant differences could be found (Fig. 4a, iv), implying that the microchannel orientation does not affect cell spreading. The diagonal microchannels are marginally less often
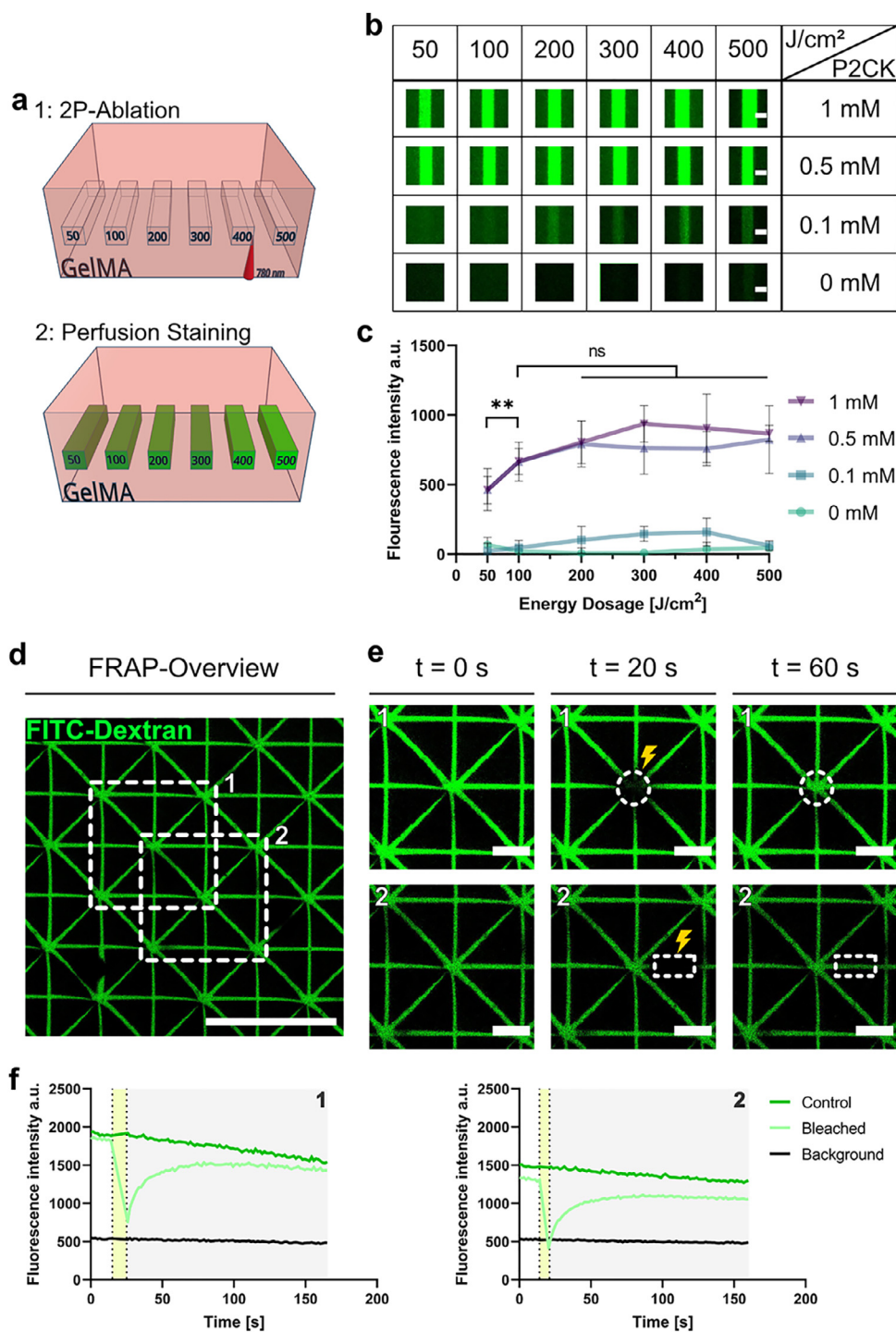
**Fig. 2.** Effect of the P2CK photosensitizer on two-photon hydrogel ablation. (a) Schematic of microchannel fabrication in 5 % GelMA hydrogels using a two-photon laser. Rectangular channels with a width and height of 5 μm are carved into the material and subsequently perfused with a fluorescent FITC-dextran solution (2 MDa) to visualize the microchannel lumen. (b) Microscopy images of stained channels, after ablation at varying dosages with different P2CK concentrations (0 mM, 0.1 mM, 0.5 mM, 1.0 mM). Scale bars, 5 μm. (c) Comparison of channel fidelity in P2CK-treated samples after photopatterning. Laser dosage E ranging from 50 J/cm² to 500 J/cm² used for ablation. Fluorescence intensity after FITC-dextran perfusion shows a significant effect of 0.5 and 1 mM P2CK on ablation over 0 and 0.1 mM P2CK ($n = 10$). Statistical analysis was performed with two-way Anova. Error bars: Mean $\pm$ SD; *$p < 0.05$. (d) Fluorescence recovery after photobleaching (FRAP) in a perfused microchannel grid. Overview of ablated (100 J/cm², 0.5 mM P2CK) microchannel grid perfused with fluorescent FITC-dextran. Regions 1 and 2 indicate FRAP sites within the grid. Scale bar, 100 μm. e) FRAP sites from d) at time points before ($t = 0$ s) and after ($t = 20$ s, 60 s) bleaching. 1: bleached junction, 2: bleached channel. Scale bar, 20 μm. f) Recovery of fluorescence intensity after bleaching site 1 (junction) and site 2 (channel). Control: unbleached positive control of fluorescently perfused grid, not bleached. Bleached: indicated bleached location within the fluorescently perfused grid. Background: unbleached background outside perfused grid.
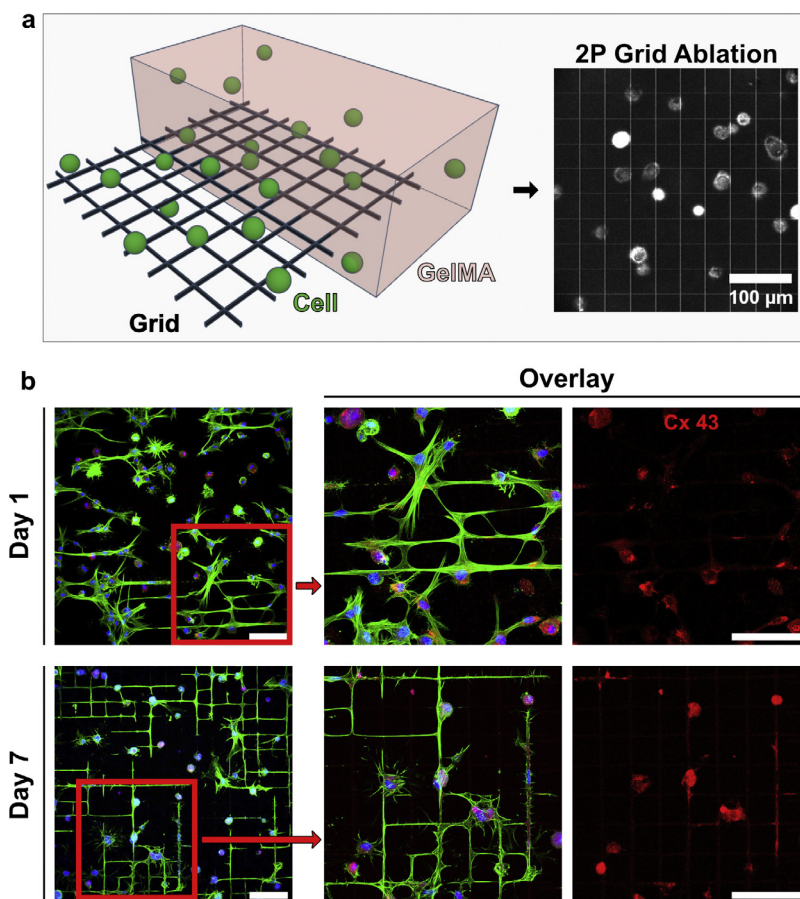
**Fig. 3.** Guided cell spreading by sensitized two-photon laser ablation into a planar microchannel grid. (a) Schematic illustrating the introduction of a 1 μm microchannel grid to a hMSC-laden 5 % GelMA hydrogel. Cells were cultured in osteogenic medium for 7 days. (b) hMSC spreading into a grid of 1 μm diameter microchannels as shown in (a) (ablated in 5 % GelMA with 400 J/cm², 0.5 mM P2CK). One week after ablation, cell protrusions stretch throughout the microchannels and resemble the grid shape. Higher magnification images show cell protrusions and a morphology with colocalized expression of the gap junction marker Connexin 43 (red). F-Actin (green), nuclei (blue), Connexin 43 (red). Scale bar, 100 μm. (For interpretation of the references to color in this figure legend, the reader is referred to the web version of this article.)

occupied, which could be related to the pixel-by-pixel laser scanning direction during the two-photon ablation process. As a result, the diagonal channel appearance shows uneven edges (Fig. S6b). Decreased cell spreading and filopodia length has been shown to be associated with increased surface roughness [33].

After 14 days of cultivation, slightly less than 50 % of the entire grid structure was occupied by cell protrusions, which is likely to increase with longer cultivation time. Assessing cell viability after 3D ablation with increasing laser dosage shows a high level of cell viability compared to unablated controls (Fig. 4b). Low-dosage ablation (100 J/cm²) resulted in 81.7 % viability, whereas high dosages led to a remarkable reduction of viability to 57.7 % (Fig. 4c).

### 3.2.3. Effect of P2CK on 3D microchannel ablation and cell guidance

By further decreasing the laser dosage to 100 J/cm², the critical impact of the photosensitizer P2CK on cell-compatible patterning can be observed (Fig. 5a). Over the course of 14 days, P2CK-treated cells that were exposed to the 3D grid can form an intricate network within the channels. In comparison, cells that were not exposed to guidance cues showed significantly less spreading (Fig. S7a, b) and thus a decreased network length per cell (Fig. 5b). Without the addition of P2CK, ablated samples showed no improved spreading and only few interactions with the grid. Therefore, the low laser dosage does not suffice to shape the grid without the presence of a two-photon photosensitizer. Within 7 days, a significant difference in network length compared to unsensitized or unablated controls was visible and measurable. Histograms

of the measured branch lengths confirmed that grid-exposed cells formed more protrusions that are longer than 30 μm, already after 7 days (Fig. 5c). As anticipated, administration of P2CK alone has no negative effect on network formation due to its low toxicity [15]. Notably, unablated samples showed only little increase in cell spreading over time, likely because cell spreading was limited by the bulk matrix. Altogether, these results demonstrate the capability of directing embedded bone cells into forming extraordinarily long, channel-permeating protrusions within a short period of time. After 14 days, the cellular networks cover a majority of the grid and clearly resemble the underlying grid morphology. Interestingly, the deposition of mineral in the form of hydroxyapatite can be observed after network formation even within the microchannels (Fig. S7c).

### 3.3. Perturbation with cell-matrix remodeling

Matrix metalloproteinases (MMP) are cell-secreted proteases for extracellular matrix remodeling that are excreted during bone formation [34,35]. We investigated the effect of broad-spectrum MMP inhibition (GM6001) on cellular network formation within the microchannel grid, due to blockage of the main gelatin-degrading enzymes such as MMP2 and MMP9 [34,36,37]. Observing cellular outgrowth via actin-nuclei staining in GM6001-treated samples showed that the cells utilize the microchannels for cell spreading despite MMP blockage, with protrusions permeating the grid (Fig. 6a). However, quantifying the network length shows that the
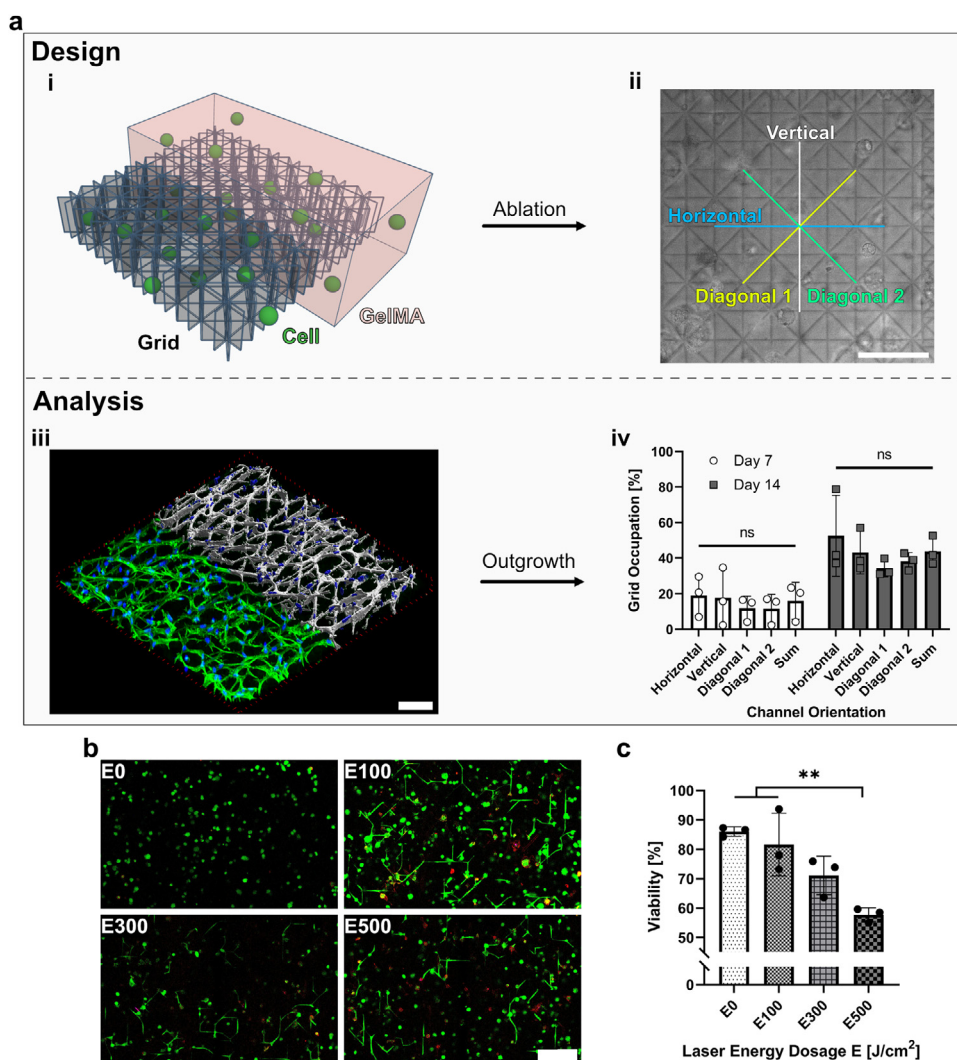
**Fig. 4.** Guided 3D cell network formation and viability within a 3D microchannel grid. (a) (i) Schematic of the size and microarchitecture of the 3D grid: microchannels (1 μm wide (x-y plane) and 30 μm deep (z-axis)) were ablated with 100 J/cm². (ii) Brightfield image after patterning: horizontal, vertical, and diagonal channels are clearly visible as lines with higher contrast. Scale bar, 100 μm. (iii) After cultivation for 14 days, cells spread into the channel network. Maximum intensity projections (MIP): 50 μm. (iv) By counting the total number of microchannels (from intersection to intersection) and dividing them by the number of protrusion-occupied microchannels, the extent of guided cell outgrowth can be quantified ($n = 3$). (b) Cell viability staining 24 h after photosensitized grid ablation with increasing laser dosage E (J/cm²). Living (green), apoptotic (red), and necrotic (blue) cells displayed in 35 μm MIP. Scale bar, 100 μm. One-way Anova, data represented as mean ± SD. (c) Quantification of the influence of different laser dosages on cell viability (manually counted). One-way Anova with multiple comparison correction. Data represented as mean ± SD; **$p < 0.001$. (For interpretation of the references to color in this figure legend, the reader is referred to the web version of this article.)

average network length per cell in patterned samples was negatively impacted by GM6001 treatment (Fig. 6b). The presence of an ablated grid seemingly only increased network length in control cultures without GM6001 treatment, regardless of grid exposure. However, branch length histograms show an increased number of longer ($\geq 50$ μm) protrusions exclusively in grid-ablated samples, even with MMP blockage (Fig. 6c). Therefore, the presence of GM6001 mostly affected the formation of shorter protrusions into the bulk matrix (Fig. S7b), which decreases the measured average network length. This indicates that inhibition of MMP-mediated matrix degradation has little effect on the cells capability to utilize the ablated microchannels. It implies that only limited MMP activity is required for cell spreading and thus low-dosage ablation sufficiently ablates the hydrogel matrix to form hollow microchannels.

Interestingly, expression of the osteogenic differentiation marker alkaline phosphatase (ALP, Fig. S8a) indicates an earlier differentiation in GM6001-treated samples opposed untreated samples. Cells exposed to the microchannel grid and MMP blockage

expressed the highest level of ALP on day 7 (Fig. S8b). While the precise role of MMPs in osteogenesis remains inconclusive, it has been shown that overexpression of MT1-MMP upregulates ALP expression [38,39]. Noteworthy, GM6001 inhibition of significantly reduced MT1-MMP expression compared to other MMPs [40]. Possibly, the synergistic effect of increased integrin binding due to microchannel presence and the relatively increased MT1-MMP expression led to upregulated ALP levels.

## 4. Discussion

We successfully employed photosensitized two-photon ablation to fabricate a grid of microchannels in the presence of bone cells, guiding cell protrusions towards the formation of an interconnected cellular network. HMSC were embedded in soft GelMA hydrogels, which served as a biocompatible platform for 3D cell culture and to perform sensitized two-photon ablation. Until now, high-resolution single-cell spatial alignment has rarely been observed in 3D matrices. Previous work was either limited to 2D sur-
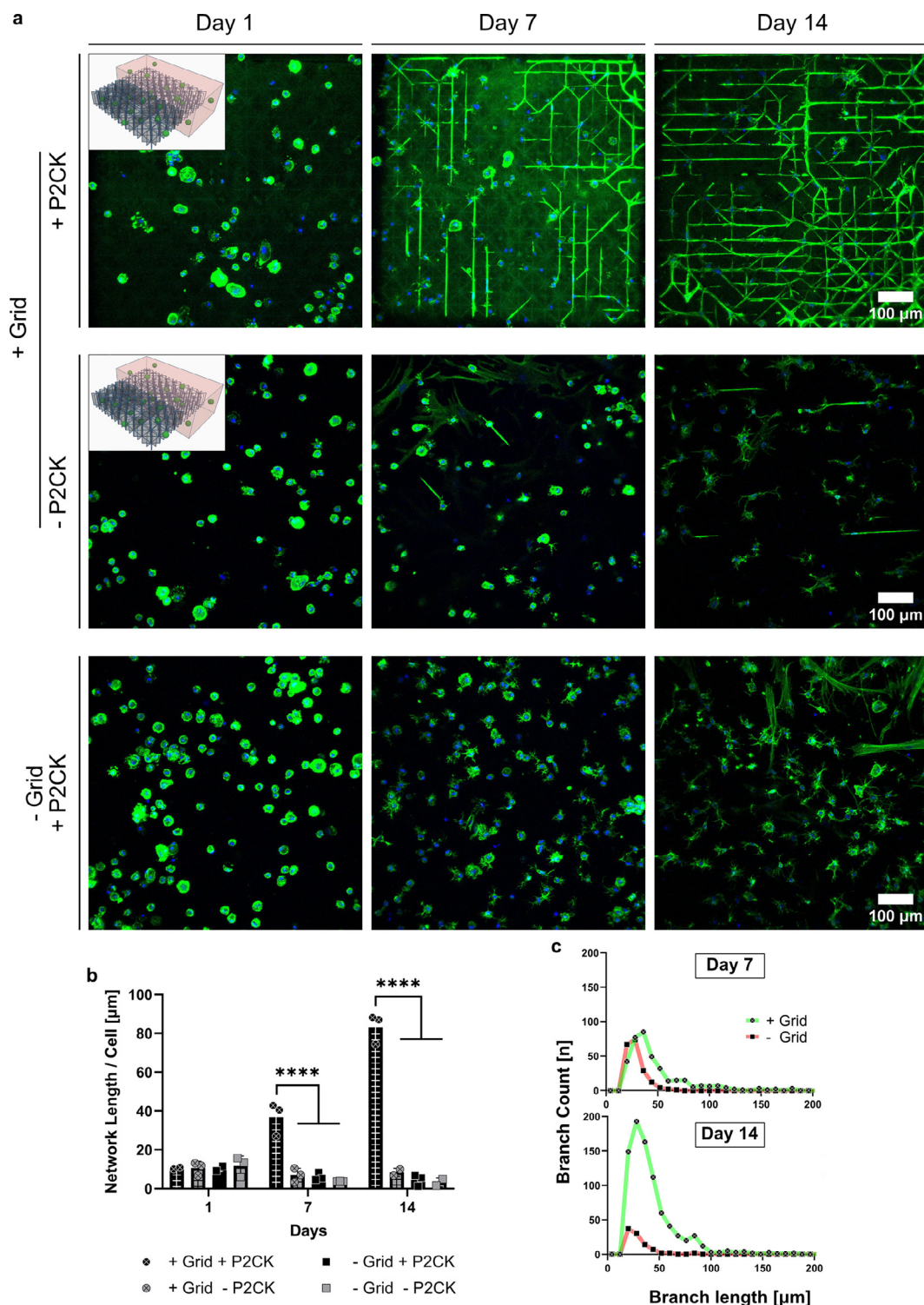
**Fig. 5.** Synergistic effects of laser ablation and P2CK photosensitization on 3D cellular network formation. Cell spreading of embedded hMSC was compared between P2CK-treated (0.5 mM) or untreated samples into a 3D-grid of 1 μm wide ($z = 30$ μm) microchannels ($E = 100$ J/cm$^2$) or the bulk hydrogel (5 % GelMA). Cells were cultured in osteogenic conditions for up to 14 days. (a) Confocal images of actin (green) and nuclei (blue) stained cells demonstrate the high degree of control over cell morphology and cellular network formation. Patterned grid with P2CK (top), patterned grid without P2CK (middle), and unablated bulk gel with P2CK (bottom). Scale bars, 100 μm. Treated samples exhibit advanced cell spreading and network formation compared to both control groups. (b) Network length normalized to the number of cells in different patterning conditions over time. After prolonged cultivation, network length increased in gels that were ablated during P2CK treatment ($n \geq 2$). Significances only displayed at located datapoints. Two-way Anova with multiple comparison correction. Data represented as mean $\pm$ SD; ****$p < 0.0001$. (c) Histograms showing the distribution by lengths of counted branches in patterned or unablated (P2CK-treated) samples. Bin size = 8. (For interpretation of the references to color in this figure legend, the reader is referred to the web version of this article.)
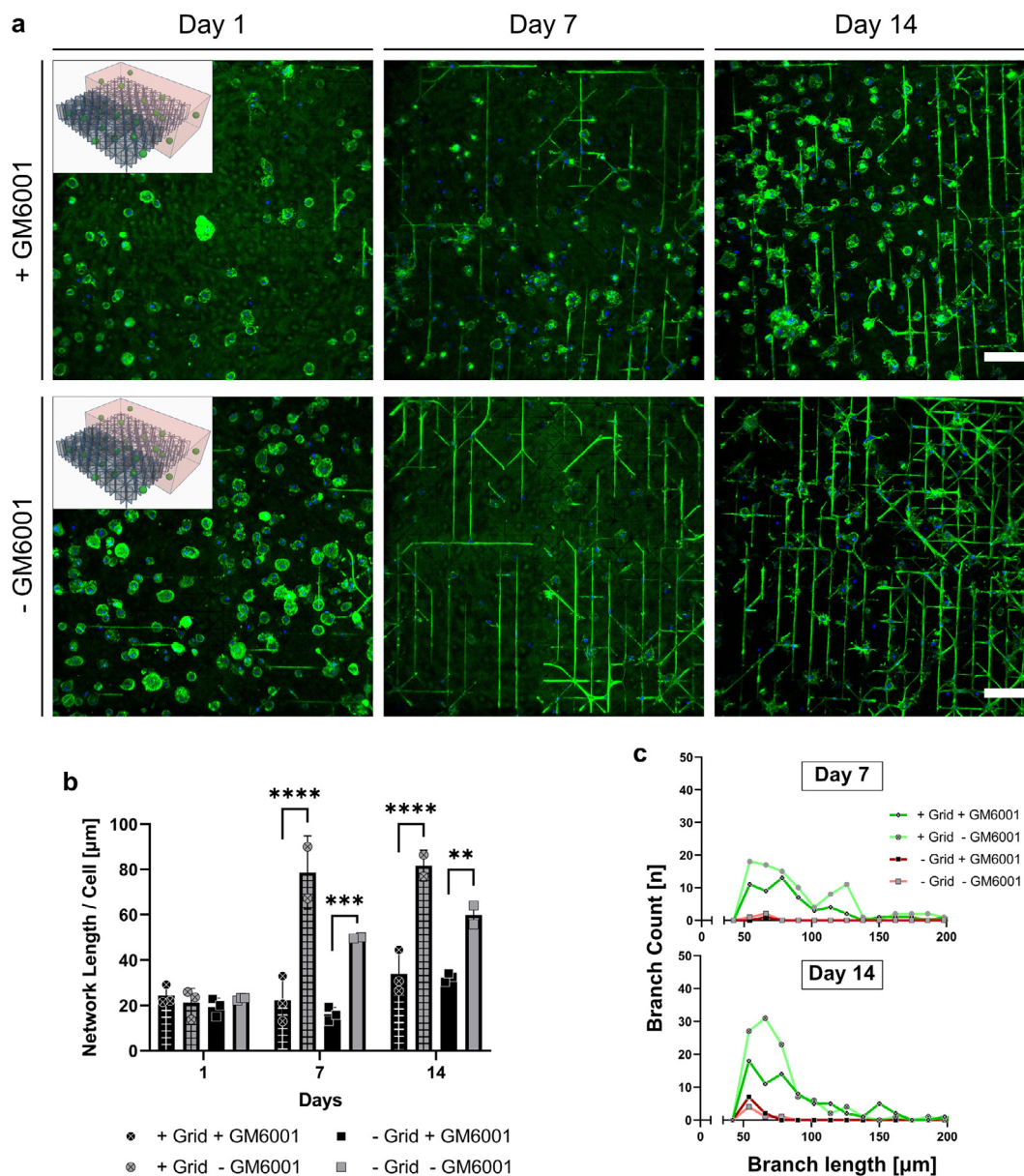
**Fig. 6.** Perturbation of cell network formation by protease inhibition. Cells were cultured in osteogenic medium for up to 14 days. (a) hMSC exposed to a microchannel grid (1 µm width, 30 µm depth) were exposed to a broad-spectrum matrix metalloproteinase (MMP) inhibitor GM6001 (10 mM). Despite MMP inhibition, grid exposure enables cells to form protrusions. Scale bars, 100 µm. (b) Quantitative analysis of protease inhibition on network formation after two-photon ablation ($n \geq 2$). GM6001 treatment reduced cell network formation compared to untreated groups. Grid presence increased average network length for untreated samples while seemingly not affecting inhibited cultures. Significances displayed at selected datapoints. Two-way Anova with multiple comparison correction. Mean ± SD; ****$p < 0.0001$; ***$p < 0.001$; *$p < 0.05$. (c) Branch length histogram shows increased number of long cellular outgrowth ($\geq 50$ µm) in ablated samples, regardless of MMP inhibition. Bin size = 12.

faces and elaborate setups [41], cellular clusters [12,18,21], or involved much larger structures to achieve visible alignment [42,43]. Faithfully guiding single cells and individual protrusions through microchannels towards the formation of cellular networks, however, has not been reported yet. So far, Xiong et al. could demonstrate single cell guidance of different cell types, but they did not succeed in fabricating elaborate networks [23].

Due to the previously reported osteogenic differentiation potential of low stiffness matrices [9] and its low mesh density, a soft GelMA (G' = 350.9 Pa, Fig. 1c) was selected. Adding 0.5 mM P2CK to the hydrogels resulted in a drastic improvement of ablation efficiency (Fig. 2), as demonstrated in perfused ablated channels and in accordance with previous work [12]. We demonstrate that a low laser dosage of 100 J/cm² is only sufficient in the presence of P2CK to enable cell-compatible laser fabrication, due to the reduced laser

exposure and thus decreased potential phototoxicity. Between 100 – 500 J/cm² little to no difference appears in degree of perfusion, indicating that a plateau and therefore the maximum level of ablation has been reached.

A 3D microchannel grid ablated with a low dosage (100 J/cm²) resulted in a more pronounced network formation over time with high cell viability (Figs. 4c and 5). Strikingly, direct exposure of the cells to the laser beam seems not to negatively impact cell viability and cell spreading. The patterning process enables reproducible fabrication of microchannels with homogenous grid occupation, regardless of channel orientation (Fig. 4d). Within the grid, cells self-organized into an interconnected network after 7 days. Cell processes are likely to further increase with longer cultivation time [8], as osteogenic differentiation drives protrusion formation. The effect of P2CK on low-dosage ablation and thus cellular net-

work formation becomes apparent in comparison with untreated groups, where only sensitized samples ablated with a grid exhibit an intricate cellular network of protrusions longer than 50 μm (Fig. 5). While the 3D grid is limited by its resemblance of continuous chasms in the z-direction, it succeeds in facilitating network formation and guiding cellular outgrowth in faithful alignment with the grid. Although administration of the MMP inhibitor GM6001 decreased the average network length in ablated samples, cells were still capable of penetrating the grid with long protrusions ($\geq$ 50 μm, Fig. 6). This implies that P2CK-mediated low-dosage ablation realizes void microchannels that require little re-modeling for cellular outgrowth. Interestingly, cell outgrowth was enhanced within the microchannels compared to the surrounding matrix, indicating their preference over the otherwise constraining matrix. Sarig-Nadir et al. previously demonstrated how neuronal cells favor outgrowth into ablated microchannels over residing in clusters [18]. Holle et al. further showed that cancer cell migration was increased in 3 μm narrow channels compared to wider channels [44]. Seemingly, confining channels promoted a change from MMP- and adhesion-dependent mesenchymal migration towards adhesion-independent ameboid migration. Interestingly, by cortical actin rearrangement ameboid migration increases the cell's ability to change shape and squeeze through confined spaces. Further investigation of cell orientation within confined spaces is needed, which could enhance our understanding of osteocyte signaling. Additionally, the cells established functional contacts through the gap junction marker (connexin 43) within the microchannels.

As two-photon ablation relies on a destructive and energy consuming process, future work requires more efficient photodegradable hydrogels [45,46]. The current simplified microchannel design approximates the length scale of the native LCN, but it does not yet resemble the intricate branching, orientation, and number of canaliculi as in vivo. Furthermore, laser-induced generation of reactive oxygen species (ROS) may interfere with the cellular metabolism. Since ROS generation is strongly dependent on applied laser dosage and the photosensitivity of selected materials, developing more efficient photodegradable hydrogels will further improve the cell-compatibility of the patterning process. This optimization is important for future high throughput screening of cellular and molecular markers in patterned hydrogel niches using bulk sequencing assays. To further validate osteocytic differentiation after network formation, prolonged cultivation time is necessary. Nonetheless, we could show that user-dictated shapes and designs of a microchannel network can be employed in the future to mimic the LCN in vitro. Adapting the shape and number of canaliculi per cell may enable researchers to investigate the effect of disease progression [7] and aging, which coincides with a decrease in osteocyte connectivity [4,47]. In future work, upscaling the ablated microchannel grid would allow for a more in-depth assessment of the bulk gene expression and osteogenic differentiation of exposed cells.

## 5. Conclusion

In conclusion, we established photosensitized two-photon laser ablation that allows to create a microchannel grid in 3D that facilitates cellular network formation within soft GelMA hydrogels. Administering the photosensitizer P2CK enabled low-dosage ablation to guide embedded bone cells into the formation of 3D networks within the grid. We demonstrated that embedded cells prefer the accessible microchannel grid over the confining bulk matrix, despite their ability to degrade and spread via proteolytic remodeling. When growing into a 3D cellular network, long protrusions permeated the microchannel grid with limited degradation activity, while expressing gap junction markers and signs of osteogenic differenti-

ation. In future, applying this method will allow to create 3D bone cell models in vitro with user-dictated morphology and function.

## Declaration of Competing Interest

The authors declare that they have no known competing financial interests or personal relationships that could have appeared to influence the work reported in this paper.

## Acknowledgements

## Supplementary materials

Supplementary material associated with this article can be found, in the online version, at doi:10.1016/j.actbio.2023.11.042.

## References

[1] L. Moroni, J.A. Burdick, C. Highley, S.J. Lee, Y. Morimoto, S. Takeuchi, J.J. Yoo, Biofabrication strategies for 3D in vitro models and regenerative medicine, Nat. Rev. Mater. 3 (5) (2018) 21–37.

[2] M.W. Tibbitt, K.S. Anseth, Hydrogels as extracellular matrix mimics for 3D cell culture, Biotechnol. Bioeng. 103 (4) (2009) 655–663.

[3] L.F. Bonewald, The amazing osteocyte, J. Bone Miner. Res. 26 (2) (2011) 229–238.

[4] L.M. Tiede-Lewis, S.L. Dallas, Changes in the osteocyte lacunocanalicular network with aging, Bone 122 (2019) 101–113.

[5] T. Moriishi, T. Komori, Osteocytes: their lacunocanalicular structure and mechanoresponses, Int. J. Mol. Sci. 23 (8) (2022).

[6] H. Hemmatian, A.D. Bakker, J. Klein-Nulend, G.H. van Lenthe, Aging, osteocytes, and mechanotransduction, Curr. Osteoporos Rep. 15 (5) (2017) 401–411.

[7] J. Klein-Nulend, R.F. van Oers, A.D. Bakker, R.G. Bacabac, Bone cell mechanosensitivity, estrogen deficiency, and osteoporosis, J. Biomech. 48 (5) (2015) 855–865.

[8] J. Zhang, J. Griesbach, M. Ganeyev, A.K. Zehnder, P. Zeng, G.N. Schadli, A. Leeuw, Y. Lai, M. Rubert, R. Muller, Long-term mechanical loading is required for the formation of 3D bioprinted functional osteocyte bone organoids, Biofabrication 14 (3) (2022).

[9] M.J. Mc Garrigle, C.A. Mullen, M.G. Haugh, M.C. Voisin, L.M. McNamara, Osteocyte differentiation and the formation of an interconnected cellular network in vitro, Eur. Cell Mater. 31 (2016) 323–340.

[10] Q. Sun, Y. Gu, W. Zhang, L. Dziopa, J. Zilberberg, W. Lee, Ex vivo 3D osteocyte network construction with primary murine bone cells, Bone Res 3 (2015) 15026.

[11] Y. Yang, M. Wang, S. Yang, Y. Lin, Q. Zhou, H. Li, T. Tang, Bioprinting of an osteocyte network for biomimetic mineralization, Biofabrication 12 (4) (2020) 045013.

[12] M. Lunzer, L. Shi, O.G. Andriotis, P. Gruber, M. Markovic, P.J. Thurner, D. Ossipov, R. Liska, A. Ovsianikov, A modular approach to sensitized two-photon patterning of photodegradable hydrogels, Angew. Chem. Int. Ed Engl. 57 (46) (2018) 15122–15127.

[13] N. Broguiere, L. Isenmann, C. Hirt, T. Ringel, S. Placzek, E. Cavalli, F. Ringnalda, L. Villiger, R. Zullig, R. Lehmann, G. Rogler, M.H. Heim, J. Schuler, M. Zenobi–Wong, G. Schwank, Growth of epithelial organoids in a defined hydrogel, Adv. Mater. 30 (43) (2018) e1801621.

[14] H. Liu, P. Chansoria, P. Delrot, E. Angelidakis, R. Rizzo, D. Rutsche, L.A. Applegate, D. Loterie, M. Zenobi-Wong, Filamented Light (FLight) biofabrication of highly aligned tissue-engineered constructs, Adv. Mater. 34 (45) (2022) e2204301.

[15] A. Ovsianikov, S. Muhleder, J. Torgersen, Z. Li, X.H. Qin, S. Van Vlierberghe, P. Dubruel, W. Holnthoner, H. Redl, R. Liska, J. Stampfl, Laser photofabrication of cell-containing hydrogel constructs, Langmuir 30 (13) (2014) 3787–3794.

[16] F. Larramendy, S. Yoshida, D. Maier, Z. Fekete, S. Takeuchi, O. Paul, 3D arrays of microcages by two-photon lithography for spatial organization of living cells, Lab Chip 19 (5) (2019) 875–884.

[17] M.R. Gullo, S. Takeuchi, O. Paul, Multicellular biohybrid materials: probing the interplay of cells of different types precisely positioned and constrained on 3D wireframe-like microstructures, Adv. Healthc. Mater. 6 (7) (2017).

[18] O. Sarig-Nadir, N. Livnat, R. Zajdman, S. Shoham, D. Seliktar, Laser photoablation of guidance microchannels into hydrogels directs cell growth in three dimensions, Biophys. J. 96 (11) (2009) 4743–4752.

[19] S.L. Jacques, A. Vogel, J. Noack, K. Nahen, D. Theisen, S. Busch, U. Parlitz, D.X. Hammer, G.D. Noojin, B.A. Rockwell, R. Birngruber, Energy balance of optical breakdown in water, Laser-Tissue Interaction IX, 1998.

[20] C.K. Arakawa, B.A. Badeau, Y. Zheng, C.A. DeForest, Multicellular vascularized engineered tissues through user-programmable biomaterial photodegradation, Adv. Mater. 29 (37) (2017).

[21] S. Sayer, T. Zandrini, M. Markovic, J. Van Hoorick, S. Van Vlierberghe, S. Baudis, W. Holnthoner, A. Ovsianikov, Guiding cell migration in 3D with high-resolution photografting, Sci. Rep. 12 (1) (2022) 8626.

[22] S. Viguet-Carrin, P. Garnero, P.D. Delmas, The role of collagen in bone strength, Osteoporos. Int. 17 (3) (2006) 319–336.

[23] Z. Xiong, H. Li, P. Kunwar, Y. Zhu, R. Ramos, S. McLoughlin, T. Winston, Z. Ma, P. Soman, Femtosecond laser induced densification within cell-laden hydrogels results in cellular alignment, Biofabrication 11 (3) (2019) 035005.

[24] K.M. Hannah, C.D. Thomas, J.G. Clement, F. De Carlo, A.G. Peele, Bimodal distribution of osteocyte lacunar size in the human femoral cortex as revealed by micro-CT, Bone 47 (5) (2010) 866–871.

[25] Z. Li, J. Torgersen, A. Ajami, S. Mühleder, X.H. Qin, W. Husinsky, W. Holnthoner, A. Ovsianikov, J. Stampfl, R. Liska, Initiation efficiency and cytotoxicity of novel water-soluble two-photon photoinitiators for direct 3D microfabrication of hydrogels, RSC Adv. 3 (36) (2013).

[26] M. Tromayer, A. Dobos, P. Gruber, A. Ajami, R. Dedic, A. Ovsianikov, R. Liska, A biocompatible diazosulfonate initiator for direct encapsulation of human stem cells via two-photon polymerization, Polym. Chem. 9 (22) (2018) 3108–3117.

[27] P.K. Jäger, Network-Quantification, 2022. https://github.com/patrickjaeger/network-quantification.git.

[28] S. Pradhan, K.A. Keller, J.L. Sperduto, J.H. Slater, Fundamentals of laser-based hydrogel degradation and applications in cell and tissue engineering, Adv. Healthc. Mater. 6 (24) (2017).

[29] X.H. Qin, X. Wang, M. Rottmar, B.J. Nelson, K. Maniura-Weber, Near-infrared light-sensitive polyvinyl alcohol hydrogel photoresist for spatiotemporal control of cell-instructive 3D microenvironments, Adv. Mater. 30 (10) (2018).

[30] A.K. Miri, H.G. Hosseinabadi, B. Cecen, S. Hassan, Y.S. Zhang, Permeability mapping of gelatin methacryloyl hydrogels, Acta Biomater. 77 (2018) 38–47.

[31] J. Gehlen, W. Qiu, G.N. Schädli, R. Muller, X.H. Qin, Tomographic volumetric bioprinting of heterocelluclar bone-like tissues in seconds, Acta Biomater. 156 (2023) 49–60.

[32] Y. Park, C. Depeursinge, G. Popescu, Quantitative phase imaging in biomedicine, Nat. Photonics 12 (10) (2018) 578–589.

[33] Y. Hou, W. Xie, L. Yu, L.C. Camacho, C. Nie, M. Zhang, R. Haag, Q. Wei, Surface roughness gradients reveal topography-specific mechanosensitive responses in human mesenchymal stem cells, Small 16 (10) (2020) e1905422.

[34] H. Nagase, G.B. Fields, Human matrix metalloproteinase specificity studies using collagen sequence-based synthetic peptides, Biopolymers 40 (4) (1996) 399–416.

[35] A. Page-McCaw, A.J. Ewald, Z. Werb, Matrix metalloproteinases and the regulation of tissue remodelling, Nat. Rev. Mol. Cell Biol. 8 (3) (2007) 221–233.

[36] R.T. Aimes, J.P. Quigley, Matrix metalloproteinase-2 is an interstitial collagenase. Inhibitor-free enzyme catalyzes the cleavage of collagen fibrils and soluble native type I collagen generating the specific 3/4- and 1/4-length fragments, J. Biol. Chem. 270 (11) (1995) 5872–5876.

[37] J. Vandooren, N. Geurts, E. Martens, P.E. Van den Steen, S.D. Jonghe, P. Herdewijn, G. Opdenakker, Gelatin degradation assay reveals MMP-9 inhibitors and function of O-glycosylated domain, World J. Biol. Chem. 2 (1) (2011) 14–24.

[38] P. Manduca, A. Castagnino, D. Lombardini, S. Marchisio, S. Soldano, V. Ulivi, S. Zanotti, C. Garbi, N. Ferrari, D. Palmieri, Role of MT1-MMP in the osteogenic differentiation, Bone 44 (2) (2009) 251–265.

[39] S.G. Almalki, D.K. Agrawal, Effects of matrix metalloproteinases on the fate of mesenchymal stem cells, Stem Cell Res. Ther. 7 (1) (2016) 129.

[40] M. Yamamoto, H. Tsujishita, N. Hori, Y. Ohishi, S. Inoue, S. Ikeda, Y. Okada, Inhibition of membrane-type 1 matrix metalloproteinase by hydroxamate inhibitors: an examination of the subsite pocket, J. Med. Chem. 41 (8) (1998) 1209–1217.

[41] M. Nikkhah, F. Edalat, S. Manoucheri, A. Khademhosseini, Engineering microscale topographies to control the cell-substrate interface, Biomaterials 33 (21) (2012) 5230–5246.

[42] H. Aubin, J.W. Nichol, C.B. Hutson, H. Bae, A.L. Sieminski, D.M. Cropek, P. Akhyari, A. Khademhosseini, Directed 3D cell alignment and elongation in microengineered hydrogels, Biomaterials 31 (27) (2010) 6941–6951.

[43] K.C. Hribar, K. Meggs, J. Liu, W. Zhu, X. Qu, S. Chen, Three-dimensional direct cell patterning in collagen hydrogels with near-infrared femtosecond laser, Sci. Rep. 5 (2015) 17203.

[44] A.W. Holle, N. Govindan Kutty Devi, K. Clar, A. Fan, T. Saif, R. Kemkemer, J.P. Spatz, Cancer cells invade confined microchannels via a self-directed mesenchymal-to-amoeboid transition, Nano Lett. 19 (4) (2019) 2280–2290.

[45] A.M. Kloxin, M.W. Tibbitt, K.S. Anseth, Synthesis of photodegradable hydrogels as dynamically tunable cell culture platforms, Nat. Protoc. 5 (12) (2010) 1867–1887.

[46] M.W. Tibbitt, A.M. Kloxin, K.U. Dyamenahalli, K.S. Anseth, Controlled two-photon photodegradation of PEG hydrogels to study and manipulate subcellular interactions on soft materials, Soft Matter 6 (20) (2010) 5100–5108.

[47] H. Hemmatian, M.R. Laurent, A.D. Bakker, D. Vanderschueren, J. Klein-Nulend, G.H. van Lenthe, Age-related changes in female mouse cortical bone microporosity, Bone 113 (2018) 1–8.